Industrial Chemistry & Materials

ROYAL SOCIETY OF CHEMISTRY

PAPER

View Article Online
View Journal | View Issue

Check for updates

Cite this: *Ind. Chem. Mater.*, 2024, **2**, 587

# Theoretical investigation of carbon dioxide adsorption on $MgH_2$ with a cobalt catalyst†

Sara Rozas,[a] Fabiana C. Gennari,[b] Mert Atilhan,[c] Alfredo Bol[de] and Santiago Aparicio*[ae]

This work presents a theoretical investigation of carbon dioxide ($CO_2$) adsorption on $MgH_2$ and its reaction (chemisorption) with cobalt doped $MgH_2$. The focus of this study is the properties and mechanisms involved in $CO_2$ adsorption on clean $MgH_2$ surfaces and the role of Co in enhancing the adsorption process. Density functional theory (DFT) calculations were performed to examine different $CO_2$ adsorption sites on the $MgH_2$ surface along with the adsorption distances, binding energies, and geometric parameters. The results indicate that physical adsorption of $CO_2$ occurs on $MgH_2$ with similar adsorption energies at different adsorption sites. The coverage effect of $CO_2$ molecules on $MgH_2$ was also investigated, revealing an increased affinity of $CO_2$ with higher surface coverage. However, excessive coverage led to a decrease in adsorption efficiency due to competing surface adsorption and intermolecular interactions. The orientation of adsorbed $CO_2$ molecules shifted from parallel to quasi-perpendicular arrangements upon adsorption, with notable deformations observed at higher coverage, which gives a hint of $CO_2$ activation. Furthermore, the study explores the $CO_2$ adsorption capacity of $MgH_2$ in comparison to other materials reported in the literature, showcasing its medium to strong affinity for $CO_2$. Additionally, the effectiveness of a single Co atom and Co clusters as catalysts for $CO_2$ adsorption on $MgH_2$ was examined. Overall, this theoretical investigation provides insights into the $CO_2$ adsorption properties of $MgH_2$ and highlights the potential of Co catalysts to enhance the efficiency of the methanation process.

Received 4th September 2023,
Accepted 21st December 2023

DOI: 10.1039/d3im00096f

rsc.li/icm

Keywords: DFT; $CO_2$ conversion; Cobalt catalyst; Charge transfer.

## 1 Introduction

Atmospheric carbon dioxide concentration reached 424.81 ppm (global mean) in June 2023,[1] which far exceeds the natural atmospheric carbon dioxide concentrations (280 ppm)[2] before the Industrial Revolution took place. This has led to severe consequences, including climate change and global warming. Carbon dioxide capture and storage, as well as carbon dioxide capture and utilisation technologies, *i.e.*, CCSs and CCUs, respectively, have been considered a suitable approach to solve this pivotal problem.[3] Among the main $CO_2$ capture procedures (pre-combustion, post-combustion, and oxyfuel combustion[4–6]), the post-combustion process is the most engineered technology as it can be retrofitted to existing power plants.[7] However, challenges remain, such as the requirement for high-performance materials or the demand

---

[a] *Department of Chemistry, University of Burgos, 09001 Burgos, Spain. E-mail: sapar@ubu.es*
[b] *National Scientific and Technical Research Council (CONICET), Bariloche Atomic Centre (CNEA), R8402AGP, S. C. de Bariloche, Río Negro, Argentina*
[c] *Department of Chemical and Paper Engineering, Western Michigan University, Kalamazoo, MI 49008-5462, USA*
[d] *Department of Physics, University of Burgos, 09001 Burgos, Spain*
[e] *International Research Center in Critical Raw Materials for Advanced Industrial Technologies (ICCRAM), University of Burgos, 09001 Burgos, Spain*

† Electronic supplementary information (ESI) available: Fig. S1 (initial dispositions of all the considered systems); Fig. S2 (optimized geometries of systems considering $nCO_2$ molecules); Table S1 ($MgH_2$ surface angle and radius deformation); Table S2 (adsorption energies for Co-catalyzed systems); Table S3 (adsorption energies for Co-catalyzed systems); Table S4 (interatomic distances between the Co atoms for the 1 to 9 cluster formation); Table S5 (interatomic distances between cobalt atoms for surface coverage); Fig. S3 (optimised geometries of Co clusters systems); Fig. S4 (optimized geometries of Co clusters systems); Fig. S5 (details of the geometric parameters of the $7Co/MgH_2$ structure); Fig. S6 (optimized geometries of $CO_2$ on Co SAC systems); Fig. S7 (optimized geometries of $CO_2$ on *n*Co-catalyzed systems); Fig. S8 (optimized geometries of $CO_2$ + $H_2$ on Co-catalyzed systems); Table S6 (Bader ionic charges of $CO_2$ adsorption on clean $MgH_2$); Table S7 (Bader ionic charges of Co adsorption on clean $MgH_2$); Table S8 (Bader ionic charges of $CO_2$ and $H_2$ adsorption on Co/$MgH_2$); Table S9 (valence Bader charge difference for $CO_2/MgH_2$ systems); Table S10 (valence Bader charge difference for $Co/MgH_2$ systems); Table S11 (valence Bader charge difference for $CO_2$/Co–$MgH_2$ systems); Table S12 ($MgH_2$ surface energies for the *k*-point testing set); Fig. S9 ($MgH_2$ surface energies as a function of the selected *k*-points). See DOI: **https://doi.org/10.1039/d3im00096f**

for energy for the high sorbent regeneration process.[8] In this process, once $CO_2$ gas is captured by the sorption material from industrial flue gases, it can be stored in suitable geological formations[9] in the case of CCS or reused in different industrial processes in the case of CCUs. This may create extra operational needs (CCUs with conversion), such as fuels or polymeric materials,[10] or be ready to use (CCUs without conversion), such as heat transfer fluid.[11]

A possible route for CCU is methane production (methanation) from captured $CO_2$ through hydrogenation. $CO_2$ methanation is one of the most relevant applications for recycling carbon dioxide, owing to its high gravimetric heat (55.5 MJ $kg^{-1}$).[12] Different means for $CO_2$ methanation have been proposed, including photocatalytic,[13] thermal catalytic,[14] or metal-catalyzed processes,[15] among others. Recent techno-economical analyses of the most mature technologies showed several drawbacks, with the main need being the development of more efficient sorbent/catalysts to allow scaling up to the industrial level.[16] A possible route for $CO_2$ methanation stands on the Sabatier reaction,[17] *i.e.*, the hydrogenation reaction of $CO_2$ to $CH_4$, which is thermodynamically favourable $\left(\Delta H^{\circ}_{298} = -165\ \mathrm{kJ\ mol^{-1}}\right)$[18] but must be catalyzed due to strong kinetics limitations. Likewise, the hydrogen required for the methanation may be provided to the chemical reactor[19] or it could be produced *in situ*. This last option could allows capturing and converting $CO_2$ simultaneously as well as ensuring the green origin of the hydrogen used.

Among the materials which can potentially be used as hydrogen sources, $MgH_2$ has shown a large hydrogen storage capacity.[20–22] Nevertheless, high hydrogenation/dehydrogenation temperatures remain technologically and economically unaffordable for large-scale application of $MgH_2$. However, Ni- and Co-additives have been shown to positively alter hydrogen absorption/desorption kinetics.[23,24] Cui *et al.*[25] confirmed that transition metal nanoparticles (NPs) of Ti, Nb, V, Co, Mo, and Ni enhance dehydrogenation performance due to a decrease in electronegativity. Dehydrogenation co-catalyzed with $MgH_2$ was reported by Gennari *et al.* showing hydrogen absorption/desorption temperatures dropping from 350 to 250 °C (ref. 26) and activation energies from 143 to 110 kJ $mol^{-1}$. Liu *et al.* reported improved hydrogen absorption/desorption performance in terms of $H_2$ temperature release (198.9 °C) and activation energies (76.66 kJ $mol^{-1}$) using Co/Pd@CNTs catalyst.[27] Therefore, taking advantage of $MgH_2$ material as a hydrogen source, $CO_2$ hydrogenation and conversion into valuable products has been assessed from an experimental point of view using $MgH_2$ as substrate.[28] Therefore, $MgH_2$ has been considered a substrate for $H_2$ supply in the $CO_2$ methanation process due to its natural capacity to release $H_2$ above 350 °C.[18] Theoretical studies have already been performed in this context; Manggada *et al.* employed an $MgH_2$ substrate for the $CO_2$ hydrogenation using a Mo-phosphonic acid catalyst to report a great reduction in the interaction energy barriers in the presence of the catalyst.[29] Cu/$ZrO_2$ system has also been evaluated in hydrogenation of $CO_2$ to methanol showing potential active reaction sites.[30] Moreover, Chen *et al.* reported DFT calculations revealing an enhanced weakening of the H–Mg surface bonds by introducing Mg

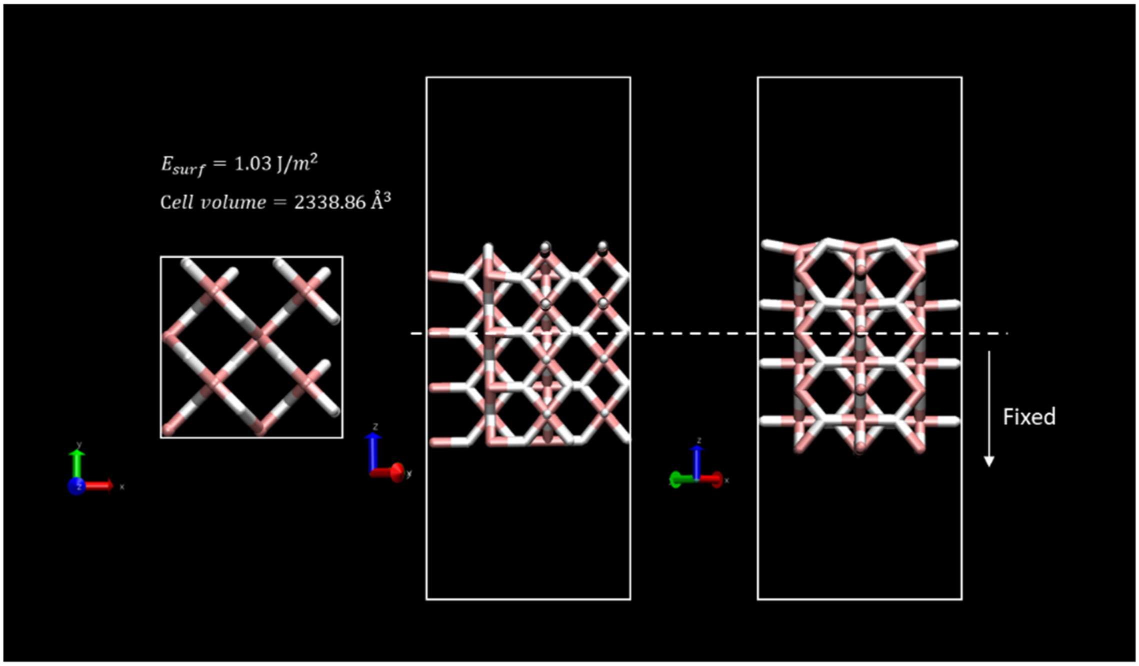

**Fig. 1** Top- and two-side-view representations of the system used in the simulations. The (0 0 1) surface energy and total volume of the optimized slab after calculation are depicted. Atom colour code: (white) hydrogen, (pink) magnesium.

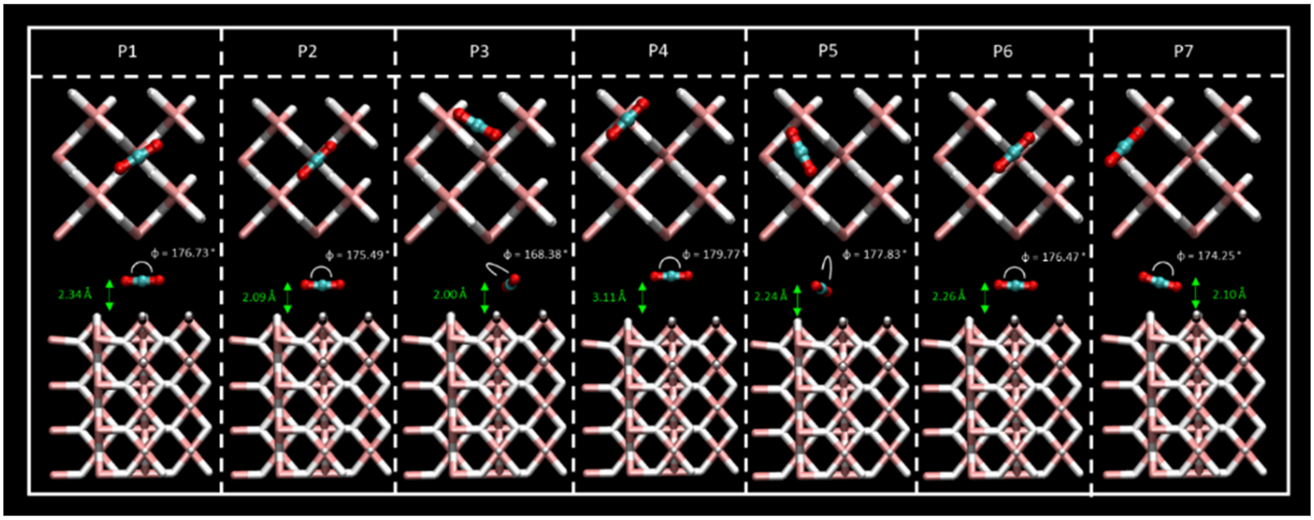

**Fig. 2** Top- and side-view of the $CO_2$ adsorption structures for the P1–P7 sites, where $CO_2$ bending angles and $CO_2$–slab distances are shown. Atom colour code: (white) hydrogen, (pink) magnesium, (red) oxygen, (blue) carbon.

vacancies, thus facilitating $CO_2$ molecule adsorption on the $MgH_2$ substrate.[31] Experimentally, Co-based catalysts for this reaction have been studied widely.[32,33] Computational studies based on theoretical models are in demand to accurately assess and evaluate active sites in materials.[34]

$CO_2$ methanation assays with $MgH_2$ substrate as a portable hydrogen medium under thermal conditions were performed in previous work on cobalt catalysts. Results showed the mechanisms for direct $CO_2$ reduction to $CH_4$ in non-catalyzed systems, however, global mechanisms of catalyzed conversion are based on the Sabatier process that is enhanced by a Co catalyst.[35] In this regard, the aim of the present work is to analyze for the first time $CO_2$–$MgH_2$ interactions and adsorption mechanisms with and without adsorbed atoms of Co. We shed light on the driving forces and electronic properties in this reaction using a theoretical approach based on the density functional theory (DFT).

## 2 Results and discussion

### 2.1 $CO_2$ adsorption on clean $MgH_2$

Different sites for $CO_2$ molecule adsorption were considered on a clean $MgH_2$ (0 0 1) surface (Fig. 1) in accordance with the position of the molecule along with different orientations. Gas molecules were placed on top of Mg atoms, on top of H atoms, and over the interatomic cavities. In this third configuration, $CO_2$ molecules were parallel to the surface (*XY* plane) with two different orientations with the aim of studying all possible interactions (Fig. S1a, ESI†). Therefore, we have considered a slab model of 8.88 × 8.88 Å; seven different DFT calculations corresponding to seven initial structures for the adsorption of a single $CO_2$ molecule were performed. Optimised geometries for all the considered systems are shown in Fig. 2, where $CO_2$ bending angles and $CO_2$–surface distances are also reported, while binding energies and further geometric parameters are presented in Table 1. Binding energies for all the considered systems are rather similar, ranging from −0.38 to −0.43 eV, except for the P4 structure, which shows the weakest interaction energy (−0.20 eV) by far. These energies are directly related to the adsorption distances, where intervals of 2.01 to 2.34 Å were observed for P1, P2, P3, P5, P6, and P7 structures and 3.11 Å for the weak P4 adsorption site. This effect may be influenced by the electronegativity difference between O–H and O–Mg atoms. The O–H electronegativity difference is smaller than that between O–Mg, leading to weaker $E_{ads}$. For all the cases, $CO_2$ intramolecular bond lengths are maintained as before the adsorption (Fig. S1c, ESI†) except for minor alterations (±0.02 Å) in P2 and P7 structures. The angle, $\varphi_{O1-C-O2}$, shows negligible bending. The bending molecule with the largest

**Table 1** Adsorption energies and geometric parameters for $CO_2$ adsorption on different surface sites (P1–P7) on $MgH_2$. The values for the configurations with the highest energy (P2 and P7) are reported in bold

| | $E_{ads}$ (eV) | $r_{C-O1}$ (Å) | $r_{C-O2}$ (Å) | $\varphi_{CO_2}$ (deg) | $r_{CO_2\text{-slab}}$ (Å) |
|---|---|---|---|---|---|
| P1 | −0.38 | 1.17 | 1.17 | 176.73 | 2.34 |
| **P2** | **−0.41** | **1.17** | **1.17** | **175.49** | **2.09** |
| P3 | −0.38 | 1.17 | 1.19 | 168.38 | 2.01 |
| P4 | −0.20 | 1.17 | 1.17 | 179.77 | 3.11 |
| P5 | −0.39 | 1.17 | 1.17 | 177.83 | 2.24 |
| P6 | −0.40 | 1.17 | 1.17 | 176.46 | 2.26 |
| **P7** | **−0.43** | **1.16** | **1.17** | **174.25** | **2.10** |

deviation from the $CO_2$ linear isolated molecule (179.97°, Fig. S1c, ESI†) is found in the P3 structure (168.38°). After DFT geometric optimisation, the $CO_2$ molecule on sites P1 and P6 underwent a reorientation, and it moved to the P2 adsorption site and showed adsorption energies (−0.38 and −0.40, respectively), molecule–surface distance (2.34 and 2.26 Å, respectively), and geometrical parameters similar to the P2 structure ($E_{ads}$ = −0.41 eV and $r_{CO_2\text{-slab}}$ = 2.09 Å). In this adsorption position, the C atom of the $CO_2$ is located in a small cavity located on top of a Mg atom on the second layer on the surface, and in the middle of two H atoms on the surface. The two O atoms of the $CO_2$ molecule point to the Mg surface atoms perpendicular to the H atoms. The final geometry of $CO_2$ at P7 is also equivalent to the P2 adsorption site, but in this case, the $CO_2$ molecule is not fully parallel to the surface, and the binding energy is slightly larger (−0.43 eV). Therefore, P2, P3, and P5 were found to be the most active sites for $CO_2$ adsorption. Furthermore, $CO_2$ molecules starting at P3 and P5 evolve to a final position, where the C atoms are placed between two H atoms on the surface and the O atoms point again toward two Mg atoms on the surface; this $CO_2$ is, however, placed over the interatomic cavity (in contrast to P1, P2, P6, and P7 structures). For the latter, binding energies, $CO_2$–surface distances, and $CO_2$ geometric parameters are similar to those reported in previous systems, where the shortest $CO_2$–surface distance was found for the P3 structure (*i.e.*, 2.00 Å). Based on the binding energy strengths, the adsorption distances, and negligible changes in $CO_2$ geometry, physical adsorption of the $CO_2$ molecule on the $MgH_2$ surface can be inferred for all the proposed adsorption sites. Results agree with those reported by Chen *et al.* who explained the viability of $CO_2$ hydrogenation through ionic lattice hydrogen atoms.[31]

To better understand the adsorption mechanism for $CO_2$ gas, the effect of coverage of different $CO_2$ molecules was considered. The full coverage limit (1 ML) was defined as 4 $CO_2$ molecules (12 atoms) on top of 12 slab surface atoms (8 hydrogen + 4 magnesium atoms). Hence, an increasing number of $CO_2$ molecules corresponding to 0.25 ML, 0.5 ML, 0.75 ML, 1 ML, and saturated 1.25 ML were added to the $MgH_2$ surface (1, 2, 3, 4, and 5 molecules, respectively) according to Fig. S1b, ESI.† Surface saturation was used to evaluate the eventual reorientation of the $CO_2$ molecules on the $MgH_2$ surface. Optimized structures are shown in Fig. S2, ESI,† and the adsorption energies (per $CO_2$ molecule) and geometric properties of each of the adsorbed $CO_2$ are reported in Table 2. An increasing affinity of $CO_2$ molecules to the $MgH_2$ surface is inferred whenever enlarging surface coverage as $E_{ads}$ scale from −0.3 to −0.4 eV (2 to 4 adsorbed molecules). This means that each molecule adsorbs more easily with an increase in coverage. Moreover, $E_{ads}$ values agree with the ones reported for a single $CO_2$ molecule (P1, P2, P3, P5, P6, and P7), leading to efficient adsorption mechanisms upon coverage. However, this behaviour is not reproduced by $CO_2$ exceeding coverage structure (1.25 ML), where the $E_{ads}$ drops to −0.25 eV (per $CO_2$ molecule). The lowering of the adsorption efficiency might be caused by the competing effects of the surface adsorption and the $CO_2$ intermolecular interactions imposed by the structural design constraints together with the non-availability of the most suitable surface adsorption sites (P1–P3 and P5–P7), and the surplus molecules interact at a less energetically favoured site (P4). Regarding the orientation of the adsorbed molecules, despite the initial position of the $CO_2$ being parallel to the surface, molecules tend to reorient after geometric optimisation toward quasi-perpendicular arrangements. This is more notable with the coverage effect. In contrast to adsorption structures with single $CO_2$ molecules, $CO_2$

**Table 2** Adsorption energy (per molecule) and geometric parameters for the adsorption of *n* $CO_2$ molecules (*n* = 2 to 5) on $MgH_2$. The values for the configuration with the highest energy (4 × $CO_2$) are reported in bold

| | *n* $CO_2$ | $E_{ads}$ (eV) | $r_{C\text{–}O1}$ (Å) | $r_{C\text{–}O2}$ (Å) | $\varphi_{CO_2}$ (deg) | $r_{CO_2\text{–}H}$ (Å) |
|---|---|---|---|---|---|---|
| 2 × $CO_2$ | 1 | −0.30 | 1.21 | 1.19 | 155.75 | 1.97 |
| | 2 | | 1.16 | 1.17 | 179.18 | |
| 3 × $CO_2$ | 1 | −0.36 | 1.28 | 1.23 | 131.50 | 1.18 |
| | 2 | | 1.16 | 1.17 | 177.39 | |
| | 3 | | 1.19 | 1.16 | 177.54 | |
| **4 × $CO_2$** | **1** | **−0.40** | **1.26** | **1.23** | **130.91** | **1.17** |
| | **2** | | **1.16** | **1.18** | **174.02** | |
| | **3** | | **1.18** | **1.17** | **171.8** | |
| | **4** | | **1.16** | **1.17** | **178.15** | |
| 5 × $CO_2$ | 1 | −0.25 | 1.28 | 1.25 | 123.94 | 1.06 |
| | 2 | | 1.17 | 1.18 | 174.76 | |
| | 3 | | 1.20 | 1.17 | 175.40 | |
| | 4 | | 1.18 | 1.17 | 173.54 | |
| | 5 | | 1.17 | 1.17 | 173.20 | |

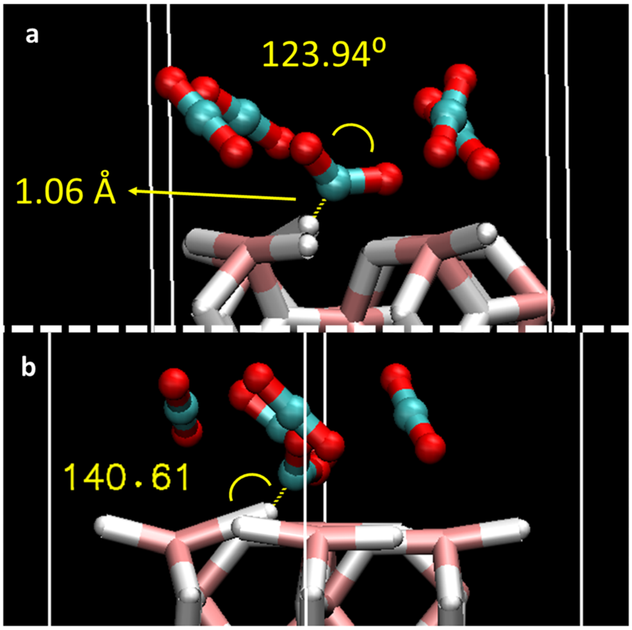

**Fig. 3** Details of the geometric parameters of (a) adsorbed $CO_2$ bending angle and C–H4 distance and (b) Mg2–H4–C contact angle related to the $CO_2$ (*n* = 1) molecule behaviour in the structure of 5 adsorbed $CO_2$ molecules.

bending angles and bond distances for all the structures vary upon adsorption (Table 2) and with $CO_2$ addition. $CO_2$ (1) molecules located on the strongest adsorption site, *i.e.*, P2, especially deform when coverage is increased, reaching a bending angle of 123.94°, bond distances of 1.28 Å, 1.24 Å, and 1.06 Å distance to the $MgH_2$ surface hydrogens, when $n$ = 5 in the coverage (Fig. 3a). At this adsorption site, slab deformation is also noticeable, especially in the $\omega_2$ angle, which changes from 157.78° in the clean slab to 149.94° after the interaction (Table S1, ESI†). Indeed, it can be inferred that a weak H-bond might be present between $H_4$ ($MgH_2$ surface) and the C atom of $CO_2$ (1) because of the bond distance (1.06 Å) and interacting angle (140.61°), although electronic charge transfer could also give rise to an adsorption mechanism that also explains chemical adsorption (Fig. 3b). A comparable situation is observed at the opposite side: $MgH_2$ H5 atom with a C–H length of 2.41 Å and contact angle of 134.34°; a slab deformation of $\omega_3$ changing from 157.78° to 174.35° was observed in this case (Table S1, ESI†). Alternate orientation of $CO_2$ molecules forming spatially perpendicular entities (non-parallel arrangement) were observed. This conformation may be adopted to avoid $CO_2$ quadrupole–quadrupole interactions, benefiting $CO_2$-slab interactions.[36] The reported effect, *i.e.*, a stronger $E_{\text{ads}}$ when coverage with $n$ $CO_2$ molecules increases, has already been described in previous literature for the $CO_2$ adsorption on rutile $TiO_2$ (1 1 0) sorbent.[37] This phenomenon will be further analysed in an upcoming section using the charge transfer phenomenon.

In summary, although the P7 position is the most stable adsorption site, adsorption energies ranging from −0.38 to −0.43 eV (except for the P4 position) indicate that the $MgH_2$ causes suitable physical adsorption of $CO_2$ molecules. The coverage effect enhances $CO_2$–$MgH_2$ surface interactions until full coverage is achieved. $CO_2$ molecular structure distortion and slab deformation upon $CO_2$ adsorption unveil possible chemical interaction between the $CO_2$ gas molecules and the $MgH_2$ sorbent. Hence, activation of the $CO_2$ molecule is demonstrated by the bending angle and bond distances of molecules and the $CO_2$–$MgH_2$ slab adsorption distances.

The $CO_2$ adsorption capacity of $MgH_2$ has been compared with that of diverse sorbent materials in the literature (Table 3). Clean $MgH_2$ slab surface shows medium to strong affinity for $CO_2$ molecules, and therefore, noteworthy $CO_2$ adsorption capacity. However, the adsorption capacities of $MgH_2$ are far from those provided by other kinds of materials, such as decorated metal–organic frameworks[38] (MOFs), doped monolayers,[39] γ-$Al_2O_3$ (1 0 0),[40] or $CuO_2$ (110),[41] as depicted in Table 3. Binding energies for the adsorption of a single $CO_2$ molecule on different materials reported in the literature, along with the DFT functional employed here, are given in Table 3.

**Table 3** Adsorption energies and computational methodology of the adsorption of one $CO_2$ molecule on the non-catalyzed surface of different materials found in the literature

| Methodology | Material | $E_{\text{ads}}$ (eV) | Ref. |
|---|---|---|---|
| **DFT-D3, PBE** | **$MgH_2$** | **−0.41** | **This work** |
| DFT, PBE | $MgH_2$ | −0.09 | 20 |
| DFT-D3, PBE | Calcite (1 0 4) | −0.38 | 42 |
| DFT, B3LYP | AlN monolayer | −0.15 | 43 |
| DFT, PBE | $TiO_2$ Brookite (2 1 0) | −0.16 | 44 |
| DFT, PBE | $TiO_2$ Anatase (1 0 1) | −0.20 | 45 |
| DFT, PBE | γ-$Al_2O_3$ (1 1 0) | −0.43 | 46 |
| DFT, PBE | γ-$Al_2O_3$ (1 0 0) | −0.80 | 32 |
| DFT-D2, PBE | Ni (1 1 0) | −0.29 | 47 |
| DFT-TS, PBE | $TiO_2$ anatase (1 0 1) | −0.42 | 48 |
| DFT, PBE | $CeO_2$ (1 1 0) | −0.24 | 49 |
| DFT, PBE | $CuO_2$ (1 1 0) | −1.22 | 50 |
| DFT-vdW-DF2, PBE | V-MOF-74s | −0.55 | 30 |
| DFT-D, PBE | $MoS_2$@GeSe monolayer | −0.96 | 31 |
| DFT-D, PBE | $TiO_2$ rutile (1 1 0) | −0.09 | 29 |
| DFT-D, PBE | $BC_3$ monolayer | −0.11 | 51 |
| DFT-D, PBE | Cu-MOF | −0.82 | 52 |

## 2.2 Co-doped $MgH_2$

To improve $CO_2$ affinity to $MgH_2$ sorbent, the Co single-atom catalyst (SAC) and Co cluster have been proposed as catalysts for $CO_2$ adsorption.[33] Adsorption energies for the different interacting sites of SAC (Fig. S1, ESI†) and Co–surface distances are reported in Table 4. For the 5 possible adsorption sites considered along the $MgH_2$ surface, C1 and C2 structures showed larger $E_{\text{ads}}$ values (−6.47 and −7.93 eV, respectively) than C3, C4, and C5 (−3.55 to −4.49 eV) (Table 4). Regarding geometry, the initial Co SAC position on C1 converged to the C2 position of Co as inferred through geometric parameters reported in Fig. 4 and Table 4. Thus, C1 and C2 sites can be considered equivalent, although the greater stability of the C2 SAC structure should be noted, which reflects the Co atom embracement by H1 and H2 atoms of the $MgH_2$ surface (Fig. 4). Despite the C1 Co–surface distances being very similar to those in C2 (Table 4), $\omega_2$ and $\omega_3$ surface angles deformation (Table S1, ESI†) from 157.78 to 132.37° and 133.91°, respectively, manifest the insertion of the Co atom in the $MgH_2$ surface structure. In contrast, for the C1 structure, $\omega_2$ and $\omega_3$ surface angles present negligible deformation (from 157.78 to 158.00° and 160.82° respectively) (Table S1, ESI†). For this reason, the C2 Co SAC structure was considered in the following section for $CO_2$ adsorption studies.

When considering multiple Co atom catalysts, stronger adsorption energies were observed on $MgH_2$ compared to

**Table 4** Adsorption energy and geometric parameters for Co atoms (SAC) at different $MgH_2$ surface sites (C1–C5). The values for the configuration with the highest energy (C2) are reported in bold

| | $E_{\text{ads}}$ (eV) | $r_{\text{Co–H1}}$ (Å) | $r_{\text{Co–H2}}$ (Å) |
|---|---|---|---|
| C1 | −6.47 | 1.52 | 1.50 |
| **C2** | **−7.93** | **1.57** | **1.57** |
| C3 | −4.49 | 2.34 | 2.17 |
| C4 | −3.55 | 1.56 | 1.56 |
| C5 | −4.49 | 1.56 | 1.56 |

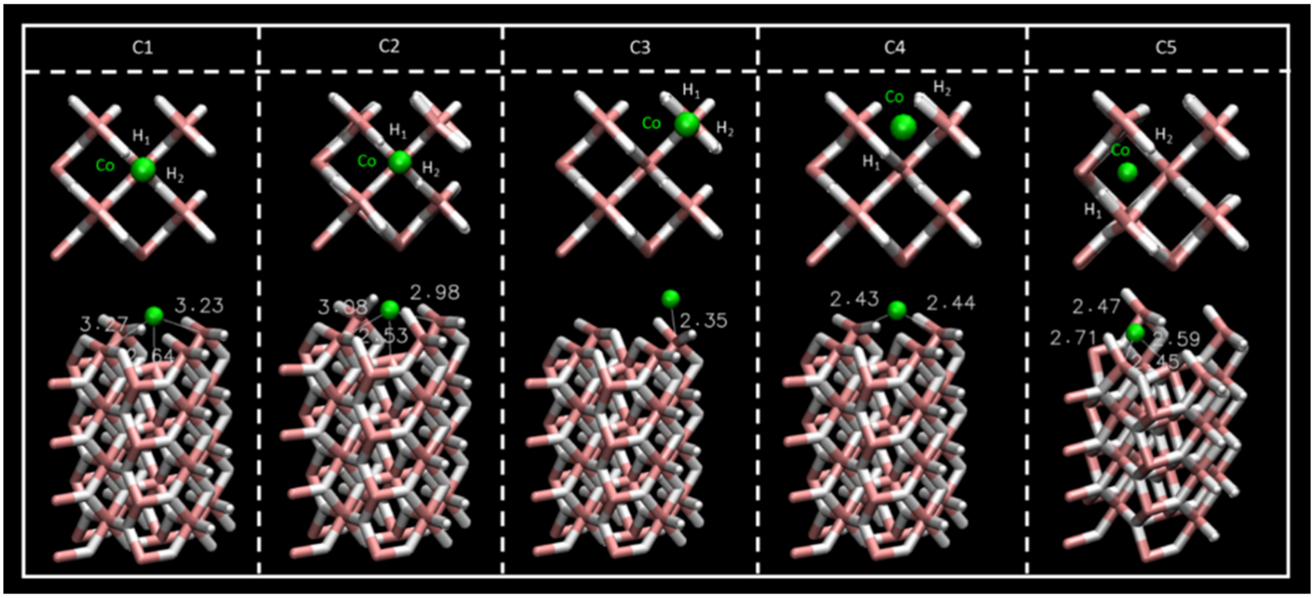

**Fig. 4** Top- and side-view of the Co SAC structures for the C1–C5 sites and Co–Mg distances. Atom colour code: (white) hydrogen, (pink) magnesium, (green) cobalt.

SAC. $E_{ads}$ (per Co atom) range from −3.09 to −10.55 eV and from −7.18 to −9.43 eV for one-by-one Co atom addition and 1/4 to full surface coverage, respectively (Tables S2 and S3, ESI†). Interatomic Co distances, which vary from 2.16 to 4.15 Å, for the one-by-one clusterization and full coverage systems (Tables S4 and S5, ESI,† respectively), agree with Co clusterization atom distances reported in the literature.[53] Catalyst adsorption on the $MgH_2$ surface causes geometric disruption of the first and second layers of $MgH_2$, and the Co embracement effect observed for the SAC structures is also reproduced for the structures with multiple Co atoms (Fig. S3 and S4, ESI†). A structure with seven Co atoms is the most energetically stable system (−10.55 eV) for *n* Co clusterization on catalyzed $MgH_2$. The geometric parameters (Table S1, ESI†) of the converged structure indicate that H4 and H5 atoms were displaced along the *x*-direction (Fig. S3, ESI†) and closely (1.64 and 1.62 Å) interacted with the central Co atom (Fig. S5, ESI†), while Mg2–H4 and Mg3–H5 distances extended from 1.82 Å to 2.05 and 2.51 Å, respectively (Table S1, ESI†). For the structure with full coverage of Co (4/4, Fig. S4, ESI†), the $E_{ads}$ were slightly weaker (−9.43 eV) than that for the cluster with 7 Co atoms (Table S3, ESI†). However, the geometric disorder of the first $MgH_2$ layer is larger, exhibiting considerable displacement of atoms and disruption of the H–Mg–H angles (Table S1, ESI†), triggering initial structural decomposition and Co atoms integration on the $MgH_2$ solid surface.

For all the reported Co catalyzing structures, large adsorption energies and non-negligible changes in surface structure were found. Therefore, the Co catalyst is intended to be capable of weakening substrate bond forces, and thus, the mechanisms of interaction between $CO_2$ molecule and $MgH_2$ surface are expected to be enhanced.

### 2.3 $CO_2$ adsorption on Co/$MgH_2$

In this section, $CO_2$ and $CO_2$ + 2/4 $H_2$ adsorption on Co/$MgH_2$ systems are discussed. First, one $CO_2$ molecule adsorption on Co SAC/$MgH_2$ was analyzed for all the SAC structures reported in the previous section. In the case of C1

**Table 5** Adsorption energy and geometric parameters for $CO_2$ adsorption for all the Co SAC sites on $MgH_2$ considered here. Both parallel (∥) and perpendicular (⊥) dispositions of the $CO_2$ molecule were considered. The values for the configuration with the highest energy (C3 $CO_2$ ∥) are reported in bold

| | $E_{ads}$ (eV) | $r_{C-O1}$ (Å) | $r_{C-O2}$ (Å) | $\varphi_{CO_2}$ (deg) | $r_{C-Co}$ (Å) | $r_{O1-Co}$ (Å) |
|---|---|---|---|---|---|---|
| C2 $CO_2$ ∥ | −6.61 | 1.20 | 1.20 | 180 | 1.98 | |
| C2 $CO_2$ ⊥ | −9.71 | 1.18 | 1.19 | 179.66 | | 1.93 |
| **C3 $CO_2$ ∥** | **−12.43** | **1.27** | **1.27** | **136.99** | **1.82** | |
| C3 $CO_2$ ⊥ | −8.86 | 1.19 | 1.18 | 178.23 | | 1.85 |
| C4 $CO_2$ ∥ | −10.17 | 1.23 | 1.29 | 140.19 | 1.81 | |
| C4 $CO_2$ ⊥ | −9.38 | 1.18 | 1.19 | 179.37 | | 1.94 |
| C5 $CO_2$ ∥ | −8.42 | 1.28 | 1.24 | 134.94 | 1.98 | |
| C5 $CO_2$ ⊥ | −7.98 | 1.17 | 1.18 | 179.85 | | 3.24 |

and C2 structures, only the C2 SAC position was considered as Co SAC spatial location is equivalent, and the energetic stability is stronger. Both the dispositions of the $CO_2$ molecule considered initially, *i.e.*, parallel and perpendicular to the surface on top of the SAC atom, manifested large $CO_2$ $E_{ads}$ in the range of −6.61 to −12.43 eV (Table 5). In the case of the C2 adsorption site, $CO_2$ adsorption energy for the parallel disposition became smaller compared to the perpendicular disposition. However, for C3, C4, and C5 structures, parallel $CO_2$ disposition showed larger interacting energies with respect to the surface. In general, larger adsorption energies (more negative values) rely on stronger interactions and greater disruption of $CO_2$ geometric parameters (Table 5). Whereas in $CO_2$ perpendicular disposition, no changes were noticed in the geometry of the gas molecules, while significant structural changes were found for the parallel disposition molecule, except for $CO_2$ adsorption on the C2 structure. $CO_2$–Co SAC distances are similar for all the structures (1.81 to 1.98 Å). The C3, C4, and C5 structures featured intense disruption of the $CO_2$ bending angles (134.94 to 140.19°) (Table 5). Therefore, despite detecting C1 and C2 as the most stable SAC structures, $CO_2$ adsorption turned out to be biased for C3, C4, and C5 (in that order), as depicted through reported $E_{ads}$ (Table 5). Adsorption on the C3 structure provides stronger interaction energy (−12.43 eV), but also the most disordered $MgH_2$ first layer.

Two adsorption mechanisms are inferred from this analysis: the first one and the most likely to occur (stronger interacting energy) is adsorption through the C atom of the $CO_2$ molecules. The second one, which is energetically weaker, is adsorption *via* the O atom with a molecular disposition perpendicular to the surface (Fig. S6, ESI†). From the former mechanism, chemical adsorption manifestation is proposed to occur based on the $CO_2$ and $MgH_2$ surface structure perturbation (Table S1, ESI†), whilst physisorption is inferred for the latter adsorption mechanism. Hence, $CO_2$ chemical activation through carbon atoms is observed as an effect that should be attributed to the Co catalyst.

$CO_2$ adsorption on a catalyst with two Co atoms on the $MgH_2$ surface presented much weaker adsorption energies for both parallel and perpendicular disposition of the gas molecule (−2.71 and −2.69 eV, respectively), which ended up converging in the same geometrical position (Fig. S7, ESI†). Although the distortion in the $CO_2$ molecular structure in the two-Co structure is slightly stronger (Table 6), the adsorption mechanisms of both the SAC and two-Co catalyst seem to behave similarly. Moderate surface deformation was observed (Table S1, ESI†).

Further investigation was carried out on the $CO_2$ adsorption mechanism on $MgH_2$ by taking into consideration $H_2$ molecules that mimic $H_2$ release from a distinct hydrogen storage substrate. Thus, 4 and 2 $H_2$ molecules, according to different experimentally reported methanation mechanisms (Sabatier process and direct $CO_2$ reduction),[26] were considered, along with one $CO_2$ molecule for the C2 SAC and two Co atoms catalyzing $MgH_2$ structures. Geometrically optimized systems displayed in Fig. S8 (ESI†) yield adsorption energies in the range of −2.61 to −3.43 eV with similar $CO_2$ molecule distortion geometries (Table 7). $CO_2$ molecule deformation is found to be in line with the previously reported adsorbed molecules, whereas $H_2$ molecules do not interact within the system as no structural changes occur on the molecules themselves and there are no significant interactions that could be observed within the $MgH_2$ surface or the $CO_2$ molecule either (Fig. S8, ESI†). It might be highlighted that for the C2 SAC structure interaction with 1 $CO_2$ and 4 $H_2$ molecules, the $CO_2$ molecule is turned parallel to the surface leading to $CO_2$–$MgH_2$ full contact, in contrast to the remaining structures (Fig. S8, ESI†). Unremarkable slab surface deformation was observed for these structures (Table S1, ESI†).

## 2.4 Insights into the charge transfer analysis and adsorption mechanisms

Charge density difference – or spatial charge redistribution – maps for the most stable aforementioned systems are shown in Fig. 5. Panel (a) represents the charge density for the clean slab; panels (b) to (d) depict the charge density difference of carbon dioxide on $MgH_2$; panels (e) to (f) show the charge density difference of Co atoms on $MgH_2$; and panels (h) to (k) show the charge density difference of $CO_2$ and $H_2$ on Co/$MgH_2$. Blue and yellow surfaces represent charge density depletion and accumulation, respectively. The difference plot slices prepared for complementary charge density in relevant

Table 6 Adsorption energy and geometric parameters for $CO_2$ adsorption on $MgH_2$ for the C2 Co SAC and the two Co atom structures. Both parallel (∥) and perpendicular (⊥) dispositions of the $CO_2$ molecule were considered. The values for the configuration with the highest energy (C3 $CO_2$ ∥ and 2 Co $CO_2$ ∥) are reported in bold

| | $E_{ads}$ (eV) | $r_{C-O1}$ (Å) | $r_{C-O2}$ (Å) | $\varphi_{CO_2}$ (deg) | $r_{C-Co1}$ (Å) | $r_{C-Co2}$ (Å) | $r_{Co1-Co2}$ (Å) |
|---|---|---|---|---|---|---|---|
| | Co SAC/C3 | | | | | | |
| **$CO_2$ ∥** | **−12.43** | **1.27** | **1.27** | **136.99** | **1.82** | | |
| $CO_2$ ⊥ | −8.86 | 1.19 | 1.18 | 178.23 | | 1.85 | |
| | 2 Co | | | | | | |
| **$CO_2$ ∥** | **−2.71** | **1.24** | **1.34** | **129.37** | **1.84** | **2.24** | **2.71** |
| $CO_2$ ⊥ | −2.69 | 1.25 | 1.33 | 130.59 | 1.83 | 2.2 | 2.81 |

**Table 7** Adsorption energy (total) and geometric parameters for $CO_2$ and $H_2$ adsorption on $MgH_2$ for the C2 Co SAC and the two Co atom structures. System with 1 × $CO_2$ molecule and 2 × $H_2$ molecules or 1 × $CO_2$ molecule and 4 × $H_2$ molecules were considered. The values for the configuration with the highest energy (1 $CO_2$ + 4 $H_2$) are reported in bold

| | $E_{ads}$ (eV) | $r_{C-O1}$ (Å) | $r_{C-O2}$ (Å) | $\varphi_{CO_2}$ (deg) | $r_{C-Co1}$ (Å) | $r_{C-Co2}$ (Å) | $r_{Co1-Co2}$ (Å) | $r_{H1-H2}$ (Å) |
|---|---|---|---|---|---|---|---|---|
| | Co SAC/C2 | | | | | | | |
| 1 $CO_2$ + 2 $H_2$ | −2.61 | 1.26 | 1.26 | 136.72 | 1.83 | — | — | 0.75 |
| **1 $CO_2$ + 4 $H_2$** | **−3.43** | **1.32** | **1.25** | **129.73** | **1.80** | — | — | **0.75** |
| | 2 Co | | | | | | | |
| 1 $CO_2$ + 2 $H_2$ | −3.10 | 1.28 | 1.28 | 136.36 | 1.90 | 1.90 | 2.66 | 0.75 |
| **1 $CO_2$ + 4 $H_2$** | **−3.43** | **1.28** | **1.29** | **136.36** | **1.90** | **1.89** | **2.66** | **0.75** |

regions of the system aid in comprehending the charge density transfer effect (Fig. 6), where red and blue colours represent maximum and minimum charge density accumulation, respectively. In panels (b) to (d) of Fig. 5, charge accumulation around oxygen and surface hydrogen atoms is outlined, whereas atomic charge depletion is observed for central carbon atoms, justifying the physisorption effect. Moderate charge transfer between $CO_2$ molecules and $MgH_2$ is shown, except for the $CO_2$ (2) molecules in panel (d), Fig. 5. Contrarily, large charge density transfer can be observed along with Co adsorption on the $MgH_2$ surface. The chemisorption of Co SAC on the $MgH_2$ surface is confirmed through strong charge interactions. An analogous effect is observed for the subsequent addition of Co atoms (Fig. 5f and g). More complex charge transfer patterns are observed in panels h to k. Combining panels (h) to (k) of Fig. 5 and 6, we can observe a double charge transfer effect: first, from the Co atoms adsorbed to the H atoms on the $MgH_2$ surface, and second, from the carbon of the $CO_2$ molecule adsorbed to the Co catalyst atoms. Hydrogen molecules do not seem to interchange charge density either with catalyzing surface or $CO_2$ molecules as no surfaces are associated with $H_2$ molecules.

Lastly, to gain insight into the $CO_2$ adsorption mechanisms, charge density transfer was investigated *via* valence Bader charges analysis. Valence electronic charges for $CO_2$ and $H_2$ molecules, first and second layers of $MgH_2$ and Co atoms were considered before and after the adsorption of the corresponding atoms/molecules (Tables S6–S8, ESI†). Next, charge transfer was calculated as the difference between the isolated surface/$CO_2$ molecule/Co atom and the valence Bader charges for the overall systems of the $CO_2$

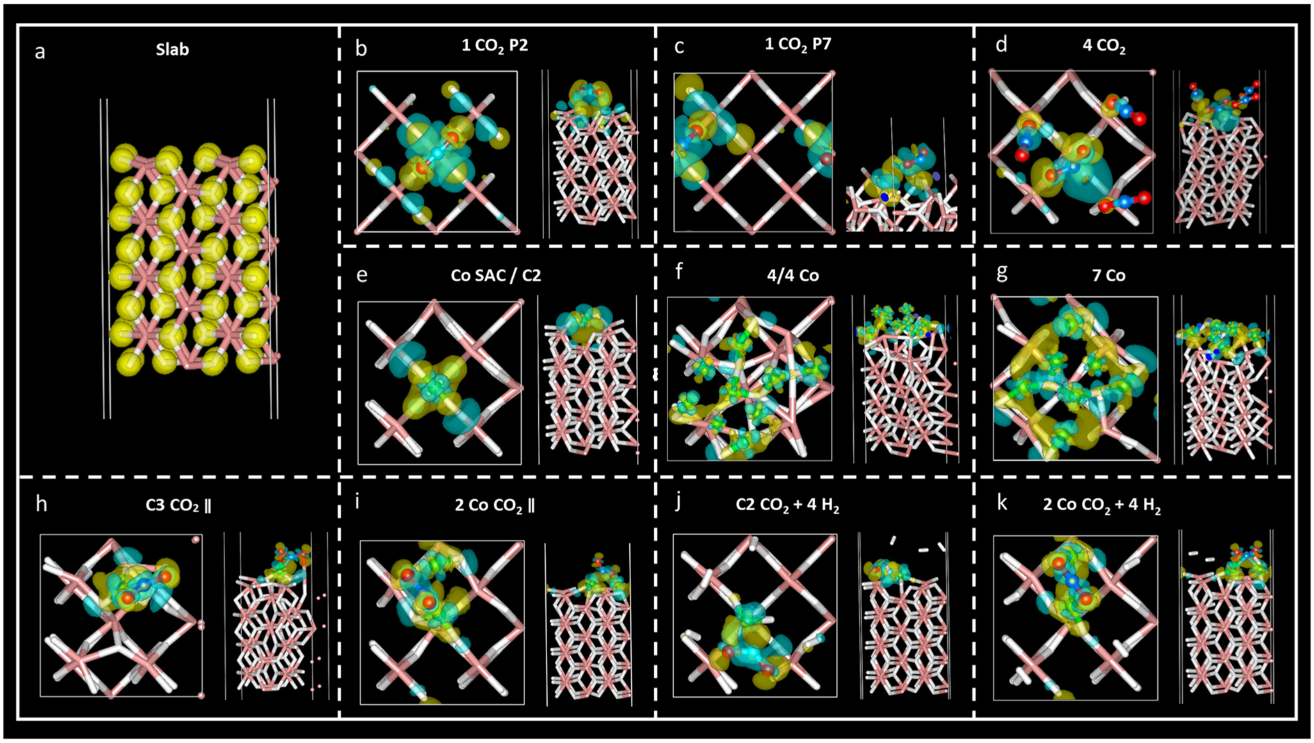

**Fig. 5** Charge density difference maps ($\rho_{system} - \rho_{slab} - \rho_{Co} - \rho_{gas}$) for the most stable structures (a–k) with the isosurface value of 0.005e. The yellow region represents charge density accumulation, while the blue region represents charge depletion.

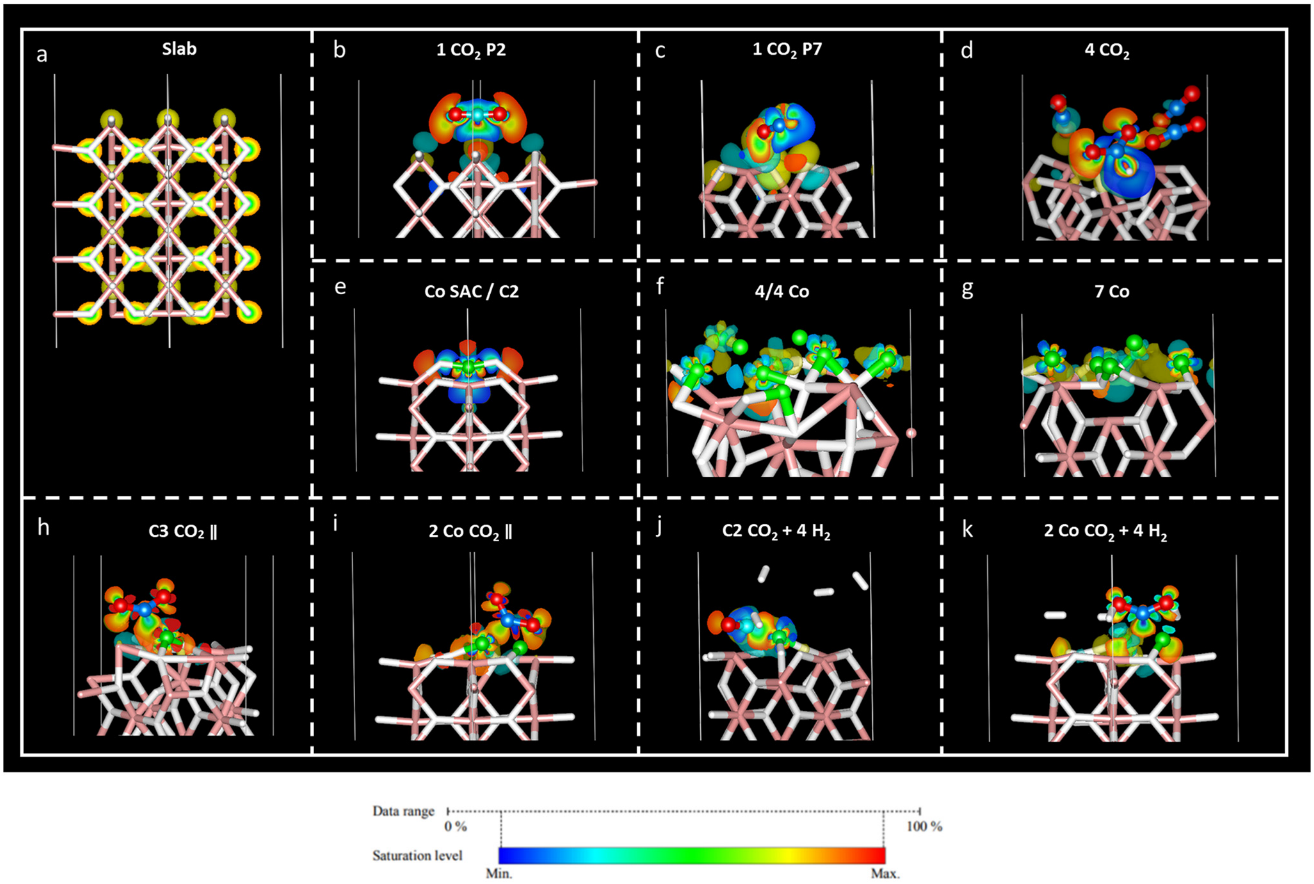

**Fig. 6** Charge density difference slice for the most stable structures (a–k) considering an isosurface value of 0.005e. Red-like colours represent charge density accumulation, while the region leaning to blue shades represents charge depletion.

molecule adsorbed on a clean $MgH_2$ surface, Co atom adsorbed on a clean $MgH_2$ surface, and $CO_2/H_2$ adsorbed on the catalysing systems (Tables S8–S10, ESI,† respectively). Positive and negative charge differences indicate charge uptake and charge loss, respectively. This means that an atom with a positive charge difference has electronic charge accumulation (negative ionic charge). Given the reported results, minor charge differences between $CO_2$ atoms and $MgH_2$ surface atoms confirm the physisorption mechanism at P2 and P7 sites (Table S9, ESI†). However, a significant charge difference was found within the $CO_2$ atoms: uptake of electronic charge by O atoms (+0.76 to +0.85) from the central C atom (which losses −1.51 and −1.67, respectively), favouring weak van der Waals interactions with the hydrogens on the $MgH_2$ surface (Table 1).

In the case of the four-$CO_2$-molecules system, physical adsorption could be inferred for $CO_2$ (1), $CO_2$ (3), and $CO_2$ (4) molecules on $MgH_2$, but chemisorption was confirmed for the $CO_2$ (2) molecule as significant charge transfer was observed between the $H_4$ and $C_1$ (2) atoms (Table S9, ESI†). This result is validated by the previously observed bending angle of the gas molecule, as well as adsorption distance (Table 2) and accumulation/depletion charge density map (Fig. 5d).

The charge difference reported for Co atoms on $MgH_2$ confirms strong interactions between the sorbent and selected catalyst as a large charge transfer was found between the hydrogen atoms on the surface and Co atoms (Table S11, ESI†). Therefore, strong adsorption of Co atoms on the $MgH_2$ surface was also corroborated by large adsorption energies and short interatomic distances (Tables 4, S2, and S3, ESI†). The charge difference of $Co_4$, $Co_5$, and $Co_9$ (Co atoms on the top of the surface H atoms), as well as $Co_4$, for seven Co and 4/4 systems, respectively, are particularly pronounced according to charge density maps (Fig. 5f and g).

Finally, the $CO_2$ and $H_2$ adsorption on the catalysis systems depicted moderate charge transfer between the $MgH_2$ surface and Co atoms combined with $CO_2$ adsorption on top of the Co atoms. In these structures, partial charge transfer from the C central $CO_2$ atom developed toward the O atoms, in parallel to partial charge transfer to the Co catalyst, leading to large ionic charge accumulation on the Co atoms. Thus, strong interactive forces between the $CO_2$ gas molecules and the catalysis surface are confirmed. Along with large $E_{ads}$ and short adsorption distances, these findings corroborate the chemical nature of the adsorption mechanism. Additionally, considerable charge density is distributed along the $CO_2$ oxygen atoms, which may lead to possible interactive sites for $H_2$ adhesion. However, despite that, low reactivity was found for $H_2$ molecules according to the reported charge transfer and charge density plots.

Based on the reported results, two main conclusions can be reached: i) high $CO_2$ adsorption capacity of $MgH_2$ was confirmed with a preferential physisorption mechanism for the clean surface and a chemisorption route for the Co-catalysed surface, and ii) no interaction could be detected between the adsorbed $CO_2$ and $H_2$ molecules.

## 3 Conclusions

In this theoretical inquiry, we systematically investigated the properties and mechanisms governing carbon dioxide ($CO_2$) adsorption on magnesium hydride ($MgH_2$) surfaces augmented with Co atoms. The focal point of our analysis was an unaltered $MgH_2$ surface and the impact of Co species on the $CO_2$ adsorption process. The findings unveiled the physical manifestation of the adsorption phenomena on the $MgH_2$ surface, whereby disparate adsorption sites are present indicating uniform adsorption energies. The influence of $CO_2$ molecular coverage on $MgH_2$ demonstrated increased affinity at enhanced surface coverage, reaching an optimal saturation point after which excessive coverage occurred and induced a decline in adsorption efficiency. Following adsorption, the orientational configuration of $CO_2$ molecules transitioned from parallel to quasi-perpendicular arrangements, accompanied by discernible deformations at heightened coverage.

In the context of comparative analyses with alternative materials, $MgH_2$ emerged as a noteworthy medium with a strong affinity for $CO_2$. Furthermore, our scrutiny of the efficacy of Co single atoms or clusters for $CO_2$ adsorption on $MgH_2$ indicated the superiority of Co single atoms for adsorption at specific sites that were reflected in heightened adsorption energies. This mechanism entails the activation of $CO_2$ molecules through perturbation of molecular properties, characterisation of $CO_2$–$MgH_2$ slab interactions, and facilitation of electronic charge transfer.

These observations collectively contribute to a deep comprehension of the underlying properties and mechanisms of $CO_2$ adsorption on $MgH_2$ in the presence of Co. Importantly, they provide pivotal insights into the initial reaction step, thereby guiding the rational design of more efficient $CO_2$ conversion technologies.

## 4 Computational methods

Quantum Espresso 6.5 software[54] with the PW package was used for DFT spin-polarised calculations. For all the atoms involved in simulations, projector augmented wave (PAW) pseudopotentials were used,[55,56] together with the revised version[57] of the PBE exchange–correlation functional.[50,58,59] Periodic boundary conditions (PBC) were applied, and dispersion forces were also included *via* the semi-empirical correction by Grimme, DFT-D3.[60] The Burai graphical user interface of Quantum Espresso was used to build the systems. The DMol3 package from the BIOVIA materials studio environment was also employed for geometry pre-optimisation and initial systems equilibration (DFT-PBE).

Magnesium hydride is characterized by a tetragonal crystal system with a $P4_2/mnm$ space group ($\alpha$-$MgH_2$).[61,62] Experimental lattice parameters are $a = b = 4.512$ Å and $c = 3.016$ Å.[63] From this data, bulk lattice was relaxed with a $k$-point Monkhorst–Pack grid[64] of 12 × 12 × 12, which was converged before considering production runs (see Table S12 and Fig. S9, ESI†) to allow the necessary energy accuracy, along with a cut-off energy of 40 Ry (544.23 eV), according to the largest value recommended in the employed pseudopotentials.

The new lattice parameters of the relaxed system were $a = b = 4.503$ Å and $c = 3.01$ Å. To mimic the bulk crystal, a 2 × 2 supercell with 4 layers of depth was generated. A surface with (0 0 1) Miller index was considered for the slab model since it is the most suitable surface regarding vacancy formation energies, and thus, the dehydrogenation process.[48,65] A twenty-Angstrom vacuum layer was set above the model slab to avoid the interaction of neighbouring $MgH_2$ cells. For all the calculations, two bottom layers of the slab were fixed to maintain crystal behaviour. Fig. 1 shows the overall simulated cell of dimensions, 8.88 × 8.88 × 30.47 Å, enclosing 96 atoms.

Surface energy, $E_{\text{surf}}$, for the clean $MgH_2$ slab was calculated according to eqn (1) because the symmetry of the two-sided slab guarantees the double counting of the surface energy. $E_{\text{bulk}}$ is the energy of the bulk $MgH_2$, and $A_{\text{slab}}$ is the surface area of a side of the calculated supercell slab model.

$$E_{\text{surf}} = \frac{E_{\text{slab}} - \left(\frac{N_{\text{slab}}}{N_{\text{bulk}}}\right)E_{\text{bulk}}}{2A_{\text{slab}}} \tag{1}$$

In this formula, $N_{\text{slab}}$ is the number of atoms on the slab, and $N_{\text{bulk}}$ is the number of atoms in the bulk material.

Once the $E_{\text{surf}}$ of the clean $MgH_2$ slab and the energy $E_{CO_2}$ of the isolated $CO_2$ molecule were computed, $CO_2$ adsorption energy ($E_{\text{ads}}$) on non-catalyzing systems was also calculated for different positions of the carbon dioxide molecule (P1–P7) as well as for different numbers of the $CO_2$ molecules ($n$ = 1–5) according to eqn (2):

$$E_{\text{ads}} = (E_{\text{surf}+nCO_2} - E_{\text{surf}} - nE_{CO_2})/n \tag{2}$$

Co-doped systems were then examined; first, by considering one cobalt atom as the SAC, C1–C5, followed by $n$ = 1–9 cobalt atoms in a growing plain cluster disposition; lastly, accounting for partial to full cobalt surface coverage layouts (1/4, 2/4, 3/4, and 4/4 of the slab surface). The energies of catalyzing systems were calculated as follows (eqn (3)):

$$E_{\text{int Co/MgH}_2} = (E_{\text{surf}+n\text{Co}} - E_{\text{surf}} - nE_{\text{Co}})/n \tag{3}$$

Accordingly, $CO_2$ adsorption energy ($E_{ads}$) on the catalyzing systems was evaluated for different dispositions of one $CO_2$ molecule (parallel and perpendicular arrangement with respect to the $MgH_2$ surface) and for one molecule of $CO_2$ and 2–4 hydrogen molecules (in agreement with 1 : 2 and 1 : 4 $CO_2/H_2$ reaction ratio) to understand interaction mechanisms. One Co SAC and two Co-catalyzed $MgH_2$ systems were considered in this section. eqn (4) describes $CO_2$ or $CO_2$ + 2/4 $H_2$ adsorption energies:

$$E_{ads} = E_{n\text{Co}/\text{MgH}_2+n\text{CO}_2+n\text{H}_2} - E_{n\text{Co}/\text{MgH}_2} - nE_{\text{CO}_2} - nE_{\text{H}_2} \quad (4)$$

For the systems in which more than one carbon dioxide molecule or hydrogen molecule is considered, the calculated adsorption energy was divided by the number of molecules to estimate the adsorption energy per molecule. In Fig. S1, ESI,† top view of the considered positions for one $CO_2$ molecule (P1–P7, Fig. S1a, ESI†) and 1 to 5 $CO_2$ molecules (Fig. S1b, ESI†) over $MgH_2$ (0 0 1) surface are shown as well as the initial bond distances and bending angle of the optimized carbon dioxide molecule (Fig. S1c, ESI†). Accordingly, SAC positions of Co (C1–C5), Co clusterization (1 Co–9 Co), and Co coverage arrangements (1/4 Co, 2/4 Co, 3/4 Co, and 4/4 Co) are shown in Fig. 1d, S1e and f, ESI,† respectively.

To elucidate the $CO_2$ adsorption mechanism and $CO_2 + H_2$ interactions over $MgH_2$ (0 0 1) surface catalyzed and non-catalyzed by Co, charge density differences obtained from electron (pseudo-) charge density quantum espresso plots were evaluated. The final spatial distribution of electronic charge density upon $CO_2/Co/H_2$ adsorption was calculated by subtracting the charge densities of the $CO_2/Co/H_2$ entity ($\rho_{\text{MgH}_2}$, $\rho_{\text{Co}}$, $\rho_{\text{CO}_2}$, $\rho_{\text{H}_2}$, respectively) from the entire final system, $\rho_{\text{Co}/\text{MgH}_2+\text{CO}_2+\text{H}_2}$ according to eqn (5):

$$\rho_{\text{final}} = \rho_{\text{sys}} - \rho_{\text{MgH}_2} - \rho_{\text{Co}} - \rho_{\text{CO}_2} - \rho_{\text{H}_2} \quad (5)$$

VESTA and VMD were used to visualize charge density differences and to evaluate charge transfer results. Bader charges of the valence electrons were also evaluated for the largest energy configurations. For this purpose, the Bader code by the Henkelman group[66–69] was employed to identify single atoms inside the system and evaluate their charge density allowing the evaluation of charge transfer phenomena upon adsorption.

## Data availability statement

The data that support the findings of this study are available from the corresponding author upon reasonable request.

## Conflicts of interest

The authors declare no conflict of interest.

## Acknowledgements

This investigation was funded by the $CO_2$ absorbing Materials Project-RISE (CO2MPRISE) which received funding from the European Union's Horizon 2020 research and innovation program under the Marie Skłodowska-Curie Grant Agreement No. H2020-MSCA-RISE-2016-CO2MPRISE-734873. We also acknowledge SCAYLE (Supercomputación Castilla y León, Spain) for providing supercomputing facilities. The statements made herein are solely the responsibility of the authors.

## References

1 Global Monitoring Laboratory, Earth System Research Laboratories, https://gml.noaa.gov/ccgg/trends/, (accessed July 2023).

2 IPCC, *Climate Change 2007. The Physical Science Basis*, Cambridge Univ. Press, Cambridge, 2007.

3 F. Kazemifar, A review of technologies for carbon capture, sequestration, and utilization: Cost, capacity, and technology readiness, *Greenhouse Gases: Sci. Technol.*, 2022, **12**, 200–230.

4 P. Markewitz, W. Kuckshinrichs, W. Leitner, J. Linssen, P. Zapp, R. Bongartz, A. Schreiber and T. E. Müller, Worldwide innovations in the development of carbon capture technologies and the utilization of CO2, *Energy Environ. Sci.*, 2012, **5**, 7281–7305.

5 N. S. Sifat and Y. Haseli, A critical review of CO2 capture technologies and prospects for clean power generation, *Energies*, 2019, **12**, 4143.

6 A. Sood, A. Thakur and S. M. Ahuja, Recent advancements in ionic liquids-based carbon capture technologies, *Chem. Eng. Commun.*, 2021, **210**, 933–954.

7 B. Dutcher, M. Fan and A. G. Russell, Amine-based CO2 capture technology development from the beginning of 2013 – A review, *ACS Appl. Mater. Interfaces*, 2015, **7**, 2137–2148.

8 A. I. Osman, M. Hefny, M. I. A. Abdel Maksoud, A. M. Elgarahy and D. W. Rooney, Recent advances in carbon capture storage and utilization technologies: A review, *Environ. Chem. Lett.*, 2021, **19**, 797–849.

9 A. Raza, R. Gholami, R. Rezaee, V. Rasouli and M. Rabiei, Significant aspects of carbon capture and storage–A review, *Petroleum*, 2019, **5**, 335–340.

10 K. M. K. Yu, I. Curcic, J. Gabriel and S. E. Tsang, Recent advances in CO2 capture and utilization, *ChemSusChem*, 2008, **1**, 893–899.

11 G. Cau, D. Cocco and V. Tola, Performance and cost assessment of Integrated Solar Combined Cycle Systems (ISCCSs) using CO2 as heat transfer fluid, *Sol. Energy*, 2012, **86**, 2985–2985.

12 R. C. Weast, *CRC handbook of chemistry and physics*, CRC Press, Boca Raton, 1973–1974.

13 U. Ulmer, T. Dingle, P. N. Duchesne, R. H. Morris, A. Tavasoli, T. Wood and G. A. Ozin, Fundamentals and applications of photocatalytic CO2 methanation, *Nat. Commun.*, 2019, **10**, 3169.

14 Z. Liu, X. Gao, B. Liu, Q. Ma, T. S. Zhao and J. Zhang, Recent advances in thermal catalytic CO2 methanation on hydrotalcite-derived catalysts, *Fuel*, 2022, **321**, 12411.

15 J. Ashok, S. Pati, P. Hongmanoram, Z. Tianxi and C. Junmei, A review of recent catalyst advances in CO2 methanation processes, *Catal. Today*, 2020, **356**, 471–489.

16 Z. Lv, H. Du, S. Xu, T. Deng, J. Ruan and C. Qin, Techno-economic analysis on CO2 mitigation by integrated carbon capture and methanation, *Appl. Energy*, 2024, **355**, 122242.

17 A. Tripodi, F. Conte and I. Rosetti, Carbon Dioxide Methanation: Design of a Fully Integrated Plant, *Energy Fuels*, 2020, **34**, 7242–7256.

18 P. Sabatier and J. B. Senderns, Mouvelles synthese du methane, *C. R. Acad. Sci.*, 1902, **134**, 514–516.

19 K. Fakumoto, W. Zhang, R. Mizoguchi, Y. Lin, C. Chai, H. Machida and K. Narinaga, CFD simulation of CO2 methanation through the Sabatier reaction in a shell-and-tube reactor incorporating phase change on the shell side, *Fuel*, 2023, **349**, 128126.

20 Q. Hou, X. Yang and J. Zhang, Review on Hydrogen Storage Performance of MgH2: Development and Trends, *ChemistrySelect*, 2021, **6**, 1589–1606.

21 E. M. Dematteis, J. Barale, M. Corno, A. Sciullo, M. Baricco and P. Rizzi, Solid-state hydrogen storage systems and the relevance of a gender perspective, *Energies*, 2021, **14**, 6158.

22 C. N. C. Hitman, M. A. A. Aziz, A. H. Ruhaimi and M. R. Taib, Magnesium-based alloys for solid-state hydrogen storage applications: A review, *Int. J. Hydrogen Energy*, 2021, **46**, 31067–31083.

23 O. Zavorotynska, I. Saldan, S. Hino, T. D. Humphries, S. Deledda and B. C. Hauback, Hydrogen cycling in γ–Mg(BH4)2 with cobalt-based additives, *J. Mater. Chem. A*, 2015, **3**, 6592–6602.

24 I. Saldan, S. Hino, T. D. Humphries, O. Zavorotynska, M. Chong, C. M. Jensen, S. Deledda and B. C. Hauback, Structural changes observed during the reversible hydrogenation of Mg(BH4)2 with Ni-based additives, *J. Phys. Chem. C*, 2014, **118**, 23376–23384.

25 J. Cui, J. Liu, H. Wang, L. Ouyang, D. Sun, M. Zhu and X. Yao, Mg-TM (TM: Ti, Nb, V, Co, Mo or Ni) core-shell like nanostructures: Synthesis, hydrogen storage performance and catalytic mechanism, *J. Mater. Chem. A*, 2014, **2**, 9645–9655.

26 M. G. Verón, H. Troiani and F. C. Gennari, Synergetic effect of Co and carbon nanotubes on MgH2 sorption properties, *Carbon*, 2011, **49**, 2413–2423.

27 M. Liu, X. Xiao, S. Zhao, M. Chen, J. Mao, B. Luo and L. Chen, Facile synthesis of Co/Pd supported by few-walled carbon nanotubes as an efficient bidirectional catalyst for improving the low temeprature hydrogen storage properties of magnesium hydride, *J. Mater. Chem. A*, 2019, **7**, 5277–5287.

28 M. L. Grasso, L. Fernández Albanesi, S. Garroni, G. Mulas and F. C. Gennari, Methane production by mechanochemical processing of MgH2-Li2CO3 as sources of H2 and CO2 at room temperature, *J. CO2 Util.*, 2020, **40**, 101209.

29 G. W. Manggada and S. Zhou, Phosphonic acid modification to molybdenum atom catalyst for CO2 hydrogenation on magnesium hydride surface, *DISTILAT: Jurnal Teknologi Separasi*, 2022, **8**, 315–324.

30 S. Polierer, J. Jelic, S. Pitter and F. Studt, On the reactivity of the Cu/ZrO2 system for the hydrogenation of CO2 to methanol: A density functional theory study, *J. Phys. Chem. C*, 2019, **123**, 26904–26911.

31 H. Chen, P. Liu, J. Li, Y. Wang, C. She, J. Liu, L. Zhang, Q. Yang, S. Zhou and X. Feng, MgH2/CuxO hydrogen storage composite with defect-rich surfaces for carbon dioxide hydrogenation, *ACS Appl. Mater. Interfaces*, 2019, **11**, 31009–31017.

32 V. Iablokow, S. K. Beaumnt, S. Alayoglu, V. V. Pushkarev, C. Specht, J. Gao, A. P. Alivisatos, N. Kruse and G. A. Somorjai, Size-controlled model Co nanoparticle catalyst for CO2 hydrogenation: Synthesis, characterization, and catalytic reactions, *Nano Lett.*, 2012, **12**, 3091–3096.

33 G. Zhou, T. Wu, H. Xie and X. Zheng, Effect of structure on the carbon dioxide methanation performance of Co-based catalyst, *Int. J. Hydrogen Energy*, 2013, **38**, 10012–10018.

34 A. Morales-García, F. Viñes, J. R. B. Gomes and F. Illas, Concepts, models, and methods in computational heterogeneous catalysis illustrated through CO2 conversion, *Wiley Interdiscip. Rev.: Comput. Mol. Sci.*, 2021, **11**(4), e1530.

35 M. L. Grasso, S. Rozas, P. A. Larochette, S. Aparicio and F. Gennari, Thermochemical transformation of CO2 for CH4 production using metal hydride and carbonates as portable sources, *Int. J. Hydrogen Energy*, 2023, **48**, 21835–24849.

36 A. J. Stone, *The theory of intermolecular forces*, Oxford University Press, New York, 1997.

37 C. Sorescu, J. Lee, W. A. Al-Saidi and K. D. Jordan, CO2 adsorption on TiO2(110) rutile: Insight from dispersion-corrected density functional theory calculations and scanning tunneling microscopy experiments, *J. Chem. Phys.*, 2011, **134**, 104707.

38 K. Lee, J. D. Howe, L.-C. Lin, B. Smith and J. B. Neaton, Small-molecule adsorption in open-site metal–organic frameworks: A systematic density functional theory study for rational design, *Chem. Mater.*, 2015, **27**, 668–678.

39 H. Yang, C. He, L. Fu, J. Huo, C. Zhao, X. Li and Y. Song, Capture and separation of CO2 on BC3 nanosheets: A DFT study, *Chin. Chem. Lett.*, 2021, **32**, 3202–3206.

40 Y. Pan, C.-J. Liu and Q. Ge, Adsorption and protonation of CO2 on partially hydroxylated γ-Al2O3 surfaces: A density functional theory study, *Langmuir*, 2008, **24**, 12410–12419.

41 A. K. Mishra, A. Roldan and N. H. Leeuw, A density functional theory study of the adsorption behavior of CO2 on CuO2 surfaces, *J. Chem. Phys.*, 2016, **145**, 4958804.

42 G. Carchini, I. Hussein, M. J. Al-Marri, R. Shawabkeh, M. Mahamoud and S. Aparicio, A theoretical study of gas adsorption on calcite for CO2 enhanced natural gas recovery, *Appl. Surf. Sci.*, 2020, **504**, 144575.

43 Y. Jiao, A. Du, Z. Zhu, V. Rudolph and S. C. Smith, Adsorption of carbon dioxide and nitrogen on single-layer aluminum nitride nanostructures studied by

density functional theory, *J. Phys. Chem. C*, 2010, **114**, 7846–7849.

44 M. M. Rodriguez, X. Peng, L. Liu, Y. Li and J. M. Andino, A density functional theory and experimental study of CO2 interaction with brookite TiO2, *J. Phys. Chem. C*, 2012, **116**, 19755–19764.

45 D. C. Sorescu, W. A. Al-Saidi and K. D. Jordan, CO2 adsorption on TiO2 (1 0 1) anatase: A dispersion-corrected density functional theory study, *J. Chem. Phys.*, 2011, **135**, 124701.

46 Y. Pan, C.-J. Liu and Q. Ge, Adsorption and protonation of CO2 on partially hydroxylated γ-Al2O3 surfaces: A density functional theory study, *Langmuir*, 2008, **24**, 12410–12419.

47 O. Mohan, Q. T. Trinh, A. Benerjee and S. H. Mushrif, Predicting CO2 adsorption and reactivity on transition metals surfaces using popular density functional theory methods, *J. Exp. Nanosci.*, 2019, **45**, 1163–1172.

48 V. Chihaia, D. A. Neacsu, V. Alexiev and D. Angelescu, Performances of the bond order interacting potentials on calculating the surface energies of MgH2 facets, Available at SSRN: **https://ssrn.com/abstract=4282784**.

49 N. Kumari, N. Sinha, M. A. Haider and S. Basu, CO2 reduction to methanol on CeO2 (1 1 0) surface: A density functional theory study, *Electrochim. Acta*, 2015, **170**, 21–29.

50 J. P. Perdew, K. Bruke and M. Ernzerhof, Generalized gradient approximation made simple, *Phys. Rev. Lett.*, 1996, **77**, 3865–3868.

51 H. Yang, C. He, L. Fu, J. Huo, C. Zhao, X. Li and Y. Song, Capture and separation of CO2 on BC3 nanosheets: A DFT study, *Chin. Chem. Lett.*, 2021, **32**, 3202–3206.

52 Q. Cui, G. Qin, W. Wang, K. R. Geethalakshmi, A. Du and Q. Sun, Novel two-dimensional MOF as promising single-atom electrocatalyst for CO2 reduction: A theoretical study, *Appl. Surf. Sci.*, 2020, **500**, 143993.

53 B. Farkas and N. H. Leeuw, Towards a morphology of cobalt nanoparticles: Size and strain effects, *Nanotechnology*, 2020, **31**, 195711.

54 P. Giannozzi, S. Baroni, N. Bonini, M. Calandra, R. Car, C. Cavazzoni, D. Ceresoli, G. L. Chiarotti, M. Cococcioni, I. Dabo, A. Dal Corso, S. de Gironcoli, S. Fabris, G. Fratesi, R. Gebauer, U. Gerstmann, C. Gougoussis, A. Kokalj, M. Lazzeri, L. Martin-Samos, N. Marzari, F. Mauri, R. Mazzarello, S. Paolini, A. Pasquarello, L. Paulatto, C. Sbraccia, S. Scandolo, G. Sclauzero, A. P. Seitsonen, A. Smogunov, P. Umari and R. M. Wentzcovitch, QUANTUM ESPRESSO: a modular and open-source software project for quantum simulations of materials, *J. Phys.: Condens. Matter*, 2009, **21**, 395502.

55 P. E. Blöchl, Generalized separable potentials for electronic-structure calculations, *Phys. Rev. B*, 1990, **41**, 5414–5416.

56 G. Kresse and D. Joubert, From ultrasoft pseudopotentials to the projector augmented-wave method, *Phys. Rev. B*, 1990, **59**, 1758–1775.

57 Y. Zhang and W. Yang, Comment on "Generalized Gradient Approximation Made Simple", *Phys. Rev. Lett.*, 1998, **80**, 890–890.

58 G. Prandini, A. Marrazzo, I. E. Castelli, N. Mounet and N. Marzari, Precision and efficiency in solid-state pseudopotential calculations, *npj Comput. Mater.*, 2018, **4**, 72.

59 K. Lejaeghere, G. Bihlmayer, T. Björkman, P. Blaha, S. Blügel, V. Blum, D. Caliste, I. E. Castelli, S. J. Clark, A. Dal Corso, S. de Gironcoli, T. Deutsch, J. K. Dewhurst, I. Di Marco, C. Draxl, M. Dułak, O. Eriksson, J. A. Flores-Livas, K. F. Garrity, L. Genovese, P. Giannozzi, M. Giantomassi, S. Goedecker, X. Gonze, O. Grånäs, E. K. U. Gross, A. Gulans, F. Gygi, D. R. Hamann, P. J. Hasnip, N. A. W. Holzwarth, D. Iuşan, D. B. Jochym, F. Jollet, D. Jones, G. Kresse, K. Koepernik, E. Küçükbenli, Y. O. Kvashnin, I. L. M. Locht, S. Lubeck, M. Marsman, N. Marzari, U. Nitzsche, L. Nordström, T. Ozaki, L. Paulatto, C. J. Pickard, W. Poelmans, M. I. J. Probert, K. Refson, M. Richter, G.-M. Rignanese, S. Saha, M. Scheffler, M. Schlipf, K. Schwarz, S. Sharma, F. Tavazza, P. Thunström, A. Tkatchenko, M. Torrent, D. Vanderbilt, M. J. van Setten, V. Van Speybroeck, J. M. Wills, J. R. Yates, G.-X. Zhang and S. Cottenier, Reproducibility in density functional theory calculations of solids, *Science*, 2016, **351**, aad3000.

60 S. Grimme, J. Antony, S. Ehrlich and H. Krieg, A consistent and accurate ab initio parametrization of density functional disersion correction (DFT-D) for the 94 elements H-Pu, *J. Chem. Phys.*, 2010, **132**, 15104.

61 J.-P. Bastide, B. Bonnetot, J.-M. Létoffé and P. Claudy, Polymorphisme de l'hydrure de magnesium sous haute pression, *Mater. Res. Bull.*, 1980, **15**, 1215–1224.

62 H. S. AlMatouk, V. Chihaia and V. Alexiev, Density functional study of the thermodynamic properties and phase diagram of the magnesium hydride, *CALPHAD: Comput. Coupling Phase Diagrams Thermochem.*, 2018, **60**, 7–15.

63 M. Bortz, B. Bertheville, G. Bötter and K. Yvon, Structure of the high pressure phase γ-MgH2 by neutron powder diffraction, *J. Alloys Compd.*, 1999, **287**, L4.

64 H. J. Monkhorst and J. D. Pack, Special points for Brillouin-zone integrations, *Phys. Rev. B*, 1976, **13**, 5188–5192.

65 W.-Y. Chen, J.-J. Tang, Z.-W. Lu, M.-X. Huang, L. Liu, C.-C. He and Y.-J. Zhao, Theoretical investigation of the surface orientation impact on the hydrogen vacancy formation of MgH2, *Surf. Sci.*, 2021, **710**, 121850.

66 M. Yu and D. R. Trinkle, Accurate and efficient algorithm for Bader charge integration, *J. Chem. Phys.*, 2011, **134**, 064111.

67 W. Tang, E. Sanville and G. Henkelman, A grid-based Bader analysis algorithm without lattice bias, *J. Phys.: Condens. Matter*, 2009, **21**, 084204.

68 E. Sanville, S. D. Kenny, R. Smith and G. Henkelman, Improved grid-based algorithm for Bader charge allocation, *J. Comput. Chem.*, 2007, **28**, 899–908.

69 G. Henkelman, A. Arnaldsson and H. Jónsson, A fast robust algorithm for Bader decomposition of charge density, *Comput. Mater. Sci.*, 2006, **36**, 354–360.